Eur. Phys. J. E (2016) **39**: 112
DOI 10.1140/epje/i2016-16112-8

THE EUROPEAN PHYSICAL JOURNAL E

Regular Article

# Discrete element modelling of sediment falling in water

Dong Wang[a], Dao Ho-Minh, and Danielle S. Tan[b]

Dept. of Mechanical Engineering, National University of Singapore, Singapore, Singapore

Received 18 October 2016
Published online: 25 November 2016 – 

**Abstract.** The Discrete Element Method (DEM) is a discrete, particle-based method commonly used in studies involving granular media, *e.g.* sediment transport, and geomechanics. It is heavily dependent on particle properties, and one important component is the force model, which relates the relative positions and velocities of the simulated particles to the forces they experience. In this paper we model a collection of lightly compacted granular material, released at a short distance above a flat base in a quiescent fluid —similar to the process whereby sediment tailings are released back into the sea during nodule harvesting. We employ different typical force models, and consider how their varying components affect the simulated outcome. The results are compared with a physical experiment of similar dimensions. We find that a realistic simulation is achieved when the force model considers the local solid fraction in the drag force, and incorporates the hydrodynamic effect of neighbouring particles. The added mass effect increases the accuracy of the outcome, but does not contribute significantly in a qualitative sense.

## 1 Introduction

The mechanics involved in fluid-solid interactions are the focal point of many research problems. The vast majority of such problems are not easily solved analytically due to factors such as, but not limited to, boundary conditions, complex and/or unsteady interfaces, complex geometry, potential chemical reactions, and the coupling/interaction at the solid-fluid interface. In the case of the solid being a collection of granular particles, then a whole new host of factors enter into the equation including the relative concentration of the particles, the size distribution of the particles and the shape(s) of the particles. Oftentimes, physical experiments are unable to provide as much information about these systems as desired and hence many researchers turn to virtual laboratories using numerical simulations to obtain the detailed information unavailable from physical experiments. Today, there are two main approaches to numerical simulations: modelling the system as a continuum (*e.g.*, computational fluid dynamics (CFD)), and employing a discrete, particle-based method (*e.g.*, dissipative particle dynamics (DPD) method [1–3] and the discrete element method (DEM) [4]).

Continuous models like CFD are very widely used and accepted, and there are several commercial software packages available to perform such simulations. CFD is based on the Navier-Stokes equations, and thus any terms and parameters involved are very closely tied to physical properties and processes like transport coefficients and convection/diffusion, etc. It has been well developed over time and applied to a great variety of problems involving different boundary conditions and levels of complexity. However one disadvantage that still remains is the fact that CFD cannot provide information at a scale smaller than its mesh resolution. Given how large the domain of interest typically is, the compromise between the level of resolution and computation cost means that information and finer details on the microscopic level are usually lost. This includes particle-level interactions and structures, which are sometimes a major point of the research investigation. In fact, particle-level characteristics which may contribute to the bulk have to be accounted for —in other words, approximated —using well-educated assumptions and constitutive relationships. These constitutive relationships are obtained either via experiments —which may be difficult for the very reason that they are on the microscale— or via a particle-based, microscale method as mentioned earlier. Thus, when modelling a multiphase system involving a granular mixture, a continuous approach may not be the most appropriate.

As the name suggests, particle-based microscale methods focus on the particle level (microscale), and approach the problem from a discrete angle. Here the driving mechanism of the simulations is the interaction between particles, *i.e.* using Newton's Laws to translate how the forces of neighbouring particles affect the motion of each individual particle. Logically then, particle properties (stiff-

[a] e-mail: wangdongntu@gmail.com
[b] e-mail: mpetds@nus.edu.sg (corresponding author)

ness, elastic modulus, shape, size, density, etc.) as well as particle interactions are of great significance. The information which these simulations can provide is thus from the microscale, but the analysis of these details over a large domain can shed light on the larger picture —the macroscale— as well as the constitutive relationships required for CFD. This makes particle-based methods a logical choice when studying granular systems, and they have indeed been employed in several areas such as granular segregation [5], avalanches and debris flow [6], sediment transport [7, 8] and fracture mechanics [9, 10]. It is possible to model the entire solid-fluid system using a combination of continuum and discrete methods (*e.g.* CFD-DEM or Lattice Boltzmann-SPH). Some researchers however choose to have a one-way coupling —that is, the fluid affects the solid motion but not vice versa. For instance the work presented in [8, 11, 12], which model the motion of sediment submerged in fluid using only the discrete element method. Unlike a simulation with two-way coupling, the fluid phase is implicitly considered through its effect on the discrete phase, which could reduce a large amount of calculation cost.

Perhaps the most significant component in any numerical simulation method is the force model, which relates the relative positions and velocities of the simulated particles to the forces they experience, and it is especially important in multiphase systems. While the particle-particle interactions are generally undisputed, the coupling between the fluid and the solid is more complicated. Firstly there is the issue of having a one-way or two-way coupling, *i.e.* modelling the fluid's effect on the solid but not the reverse, or modelling the mutual effects of both phases on each other. Then there is the host of fluid-solid interaction forces which are modelled in various combinations in numerical simulations. These forces include, but are not limited to, viscous drag, pressure gradient forces, added mass (*i.e.* virtual mass), lift and the Basset force. When modelling a granular mixture, there is an additional complication, the effect of local concentration. In other words, the presence of neighbouring particles (and their proximity) has a significant effect on how the surrounding fluid influences the motion of any one particle. Attempts to account for this have been made by modifying the drag force on individual particles, the local fluid viscosity, or various other properties of the particles and/or fluid.

Stokes' drag is a well-known and widely accepted model for laminar flows with low Reynolds number. A modification was proposed to the viscosity term, as a function of the local particle concentration [13]. Alternatively, Di Felice's drag force model [14] for a fluid-multiparticle interaction system adds a voidage exponent to the hydrodynamic drag force expression. This exponent has a constant value in both established laminar and turbulent regimes, but varies with the particle Reynolds number during the transition regime. The correlation of Wen and Yu [15] and Ergun's equation [16] are (semi-)empirical correlations for drag obtained using experimental bed pressure drop data of stationary beds. Other research has been conducted to develop drag force correlations further ([17] and [18]).

Likewise, there are a few added mass models used to account for different concentrations of solid particles. The added mass force represents the force required by a particle to accelerate the fluid surrounding it, and is typically modelled as an increase in the effective mass of the particle. In most studies involving sand and water, the added mass coefficient was assumed to be a constant 0.5, the theoretical value for a sphere moving in an unbounded fluid [19]. A modification was derived for the added mass which depends on the local particle fraction [13]. Likewise, the added mass in the dilute limit was calculated and expressions depending on the local concentration were found [20, 21].

The many force models employed today are of varying complexity and suitability to different problems, and often they have to be modified specifically for the situation. How rigid particles falling through a viscous fluid at low Reynolds number broke up was studied using a two-way coupling and Stokes' drag [22]. A coupled CFD-DEM method to investigate the fluid-particle interaction in mining and geotechnical engineering was presented [23], in which Di Felice's drag force model [14] was used. Numerical simulations of a gas-liquid-solid system were conducted including gravity, far-field pressure, Ergun [16] and Wen and Yu [15] drag equations, lift force as well as added mass forces [24]. The fluidization in a micro-reactor was studied using the Zuber equation [13] for the added mass in his numerical models [19].

One major issue in modelling is the balance between the complexity of the force model and the computation time cost. There is always the question of how encompassing a force model has to be to capture a sufficient amount of the physics involved, while simultaneously balancing the computational time and power needed. Given the various reported force models in the literature, we believe that a good model for the fluid force should include drag, added mass, and —for a cluster of solids— disturbance from neighbours. Their relative significance is unknown however, as well as possible dependence on local concentration.

Here we use DEM to model a collection of lightly compacted granular material, released at a short distance above a flat base in a quiescent fluid. We employ different typical force models based on the likely components identified above, and consider how their varying components affect the simulated outcome. We find that a realistic simulation is achieved when the force model considers the local solid fraction in the drag force, and incorporates the hydrodynamic effect of neighbouring particles. Including the added mass force increases the accuracy of the outcome, but does not contribute significantly qualitatively.

This paper is laid out as follows: we outline the physical experiment setup and corresponding results in sect. 2. Section 3 contains details on the numerical simulations — a brief description of the setup and boundary conditions of the DEM simulation, the different force models employed in this paper, and the numerical simulation results. The overall results are discussed in sect. 4.

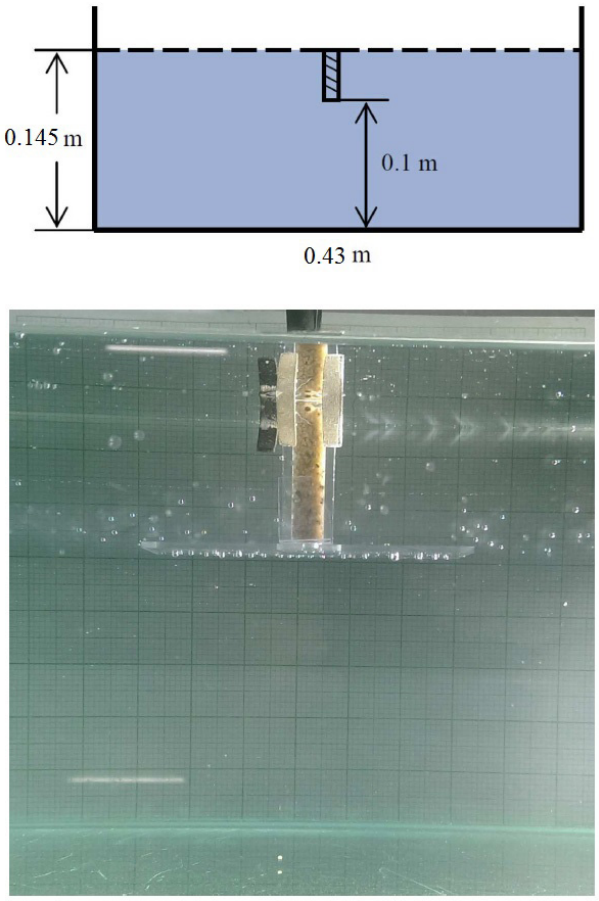


**Fig. 1.** Physical experiment: sketch and photograph. The lightly compacted sand is released underwater, at a height of 0.1 m above the floor of the tank.

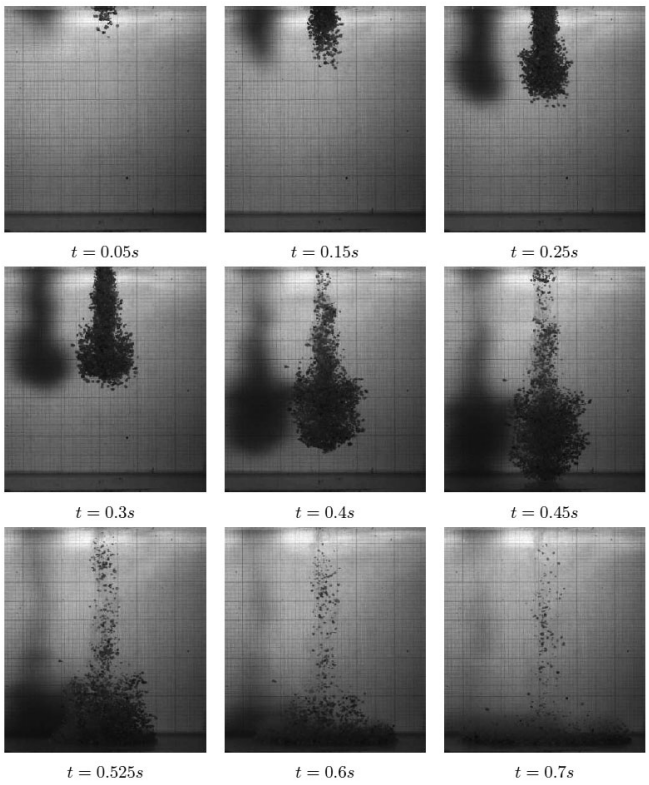


**Fig. 2.** Snapshots of the physical experiment ($t = 0.05$ to 0.7 s).

## 2 Physical experiment

### 2.1 Experimental setup

This section describes the physical experiment carried out as a reference for the simulations. The main objective here is to identify significant characteristics exhibited during the underwater dispersion process, which we can then use to verify whether our simulations have contained the essential physics. We acknowledge that quantitative characteristics like the settling time, evolution of the dispersed sediment cloud with time as well as the bulk velocity are also important. However, we believe that the simulations must first and foremost be able to capture the qualitative behaviour; only later can the quantitative behaviour be fine-tuned. Thus the emphasis here is on the qualitative rather than the quantitative.

Figure 1 shows a sketch and photograph of the experimental setup. We used a tank (interior cross-section 0.43 m by 0.195 m, height 0.25 m) with glass walls. Graph paper lined the base and back wall of the tank, for ease of measurements. Two rulers were also fixed in the tank —one to the back wall, and one at the point where sand would be released— to account for parallax error. The tank was filled with water (at room temperature) to a depth of 14.5 cm. The open-ended perspex sand container is held in place with a retort stand, on top of a perspex plate with a sliding panel, at 10 cm above the base of the tank. The panel is slid to the side to allow the sand to fall through.

Silica W7 sand (average diameter 1 mm) purchased from River Sands Australia was used. The sand was first packed compactly into the perspex container and then submerged in the tank. Once the water was relatively undisturbed again, the sand was released into the water.

We used a Photron Fastcam SA5 to record the dispersion and settling process. The photographs from figs. 2 and 3 were extracted from the video. The experiment was repeated several times, and the average settling time and horizontal spreading distance were obtained.

### 2.2 Experimental results

Figure 2 shows one of the experiments in progress, with the images advancing in time from $t = 0$ to 0.7 s (left to right, then top to bottom). We can make the following observations from fig. 2:

- In the first three images, the area of the sand cluster increases slightly over time. This is due to the sand expanding from its initially compacted state.
- Comparing the second row of snapshots, we see that there is the clear formation of a spherical cluster which

increases in size. In particular, particles in the centre fall faster and further than those on the peripheries of the cluster, before being recirculated up and along the edges of the cluster. This implies that particles with higher local concentration move faster than those with lower local concentration.

– The horizontal spreading (which we call "xrange") increases from $t = 0.5$ to 0.6 s, causing the spherical shape to become slightly distorted and wider at the base. This phenomenon is caused by the particles approaching the wall, and is accounted for in model 4 by the introduction of the "mirror" particles.
– In the last two snapshots, we observe that there is no significant bouncing as the particles reach and settle on the tank base.

The final spread area of the sand was measured for three sets of experiments. The typical final settled shape is shown in fig. 3, which is a circular ring surrounding a smaller circular pile. In fig. 3, all the particles fell in a circle of radius 40 mm, with the majority within a circle of 32 mm radius. Considering the other two sets of experimental results (not shown here), the sand falls in a circle of 38–42 mm, with the majority in a circle with radius 6–8 mm smaller.

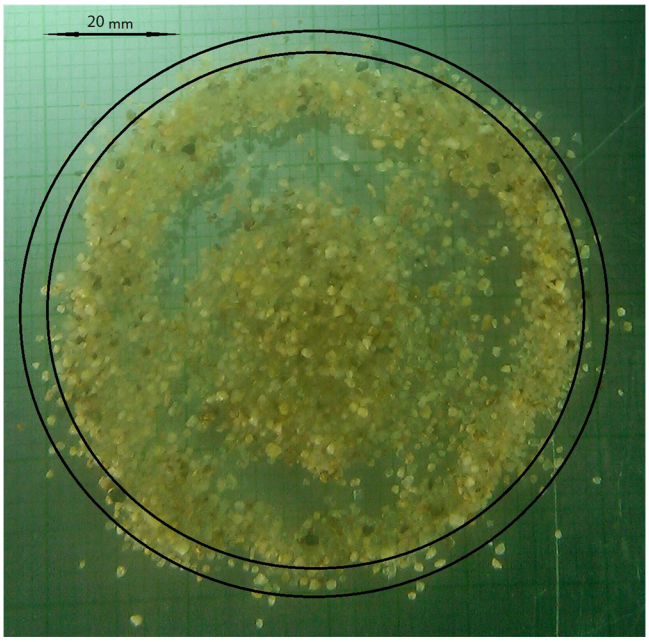


**Fig. 3.** Top view of the sand settled on the floor of the water tank. The smaller circle includes ≈ 90% of the particles, while the larger circle denotes the maximum spread area.

## 3 Numerical simulations

In this section we describe the simulated system, and the related simulation parameters and boundary conditions. To investigate the various force models described in sect. 3.3, the simulated system will be a lightly compacted granular mixture released underwater, a short distance from the base. The simulation method of choice is DEM, which was first introduced by Cundall and Strack [4] to study granular dynamics. Specifically, we use the open-source software LAMMPS [25] to perform the DEM simulations.

### 3.1 Discrete Element Method (DEM) details

The general calculation procedure during each time-step begins with the relative positions and velocities of all the particles in the simulation. This information is known from the previous time-step, and is used to determine 1) which particles are neighbours, and 2) how much contact (overlap) they have with each other. The amount of force exerted on each particle by its neighbour is then determined by the contact force model (part of which is outlined in sect. 3.3).

In our DEM simulations we employ the soft-sphere contact force model for inter-particle contacts, *i.e.* the particles are assumed soft enough that they are able to undergo deformation when they are in contact with each other. From Hertzian contact theory, the relationship between the deformation (overlap) is related to the repulsive force between contacting particles as follows:

$$\mathbf{F}_n = -k_n \delta_n^{1/2}\, \mathbf{n}_{ij} - \gamma_n \delta_n^{1/4} \dot{\boldsymbol{\delta}}_n \qquad (1)$$

**Table 1.** Formulae for calculating stiffness and damping coefficients.

| Variable | Formulae |
|---|---|
| $k_n$ | $(4/3)\sqrt{R_{\text{eff}}}E_{\text{eff}}$ |
| $k_t$ | $8\sqrt{R_{\text{eff}}}G_{\text{eff}}$ |
| $\gamma_n$ | $\alpha\sqrt{m_{\text{eff}}k_n}$ |
| $\gamma_t$ | $\alpha\sqrt{m_{\text{eff}}k_t}$ |
| $R_{\text{eff}}$ | $(1/R_1 + 1/R_2)^{-1}$ |
| $E_{\text{eff}}$ | $[(1-\nu_1^2)/E_1 + (1-\nu_2^2)/E_2]^{-1}$ |
| $G_{\text{eff}}$ | $[2(1+\nu_1)(2-\nu_1)/E_1 + 2(1+\nu_2)(2-\nu_2)/E_2]^{-1}$ |
| $m_{\text{eff}}$ | $(1/m_1 + 1/m_2)^{-1}$ |

and

$$\mathbf{F}_t = \min\left\{-k_t\delta_n^{1/2}\boldsymbol{\delta}_t - \gamma_t\delta_n^{1/4}\dot{\boldsymbol{\delta}}_t,\ \mu^c\mathbf{F}_n\right\}. \qquad (2)$$

$\mathbf{F}_n$ and $\mathbf{F}_t$ are the normal and tangential forces generated between a pair of contacting particles $i$ and $j$. $k_n$, $k_t$, $\gamma_n$ and $\gamma_t$ are the stiffness and viscoelastic damping coefficients in the normal and tangential directions, respectively, which are related to the particles material properties (see table 1). $\boldsymbol{\delta}_n$ and $\boldsymbol{\delta}_t$ are the normal and tangential components of the overlap vector (dots overhead denote rate of change with time) with magnitude $\delta$, $\mathbf{n}_{ij}$ is the unit vector acting along the line from the centre of particle $j$ to the centre of particle $i$, and $\mu^c$ is the material friction coefficient.

Newton's Laws then relate the resultant force and torque on each particle to their acceleration, which is

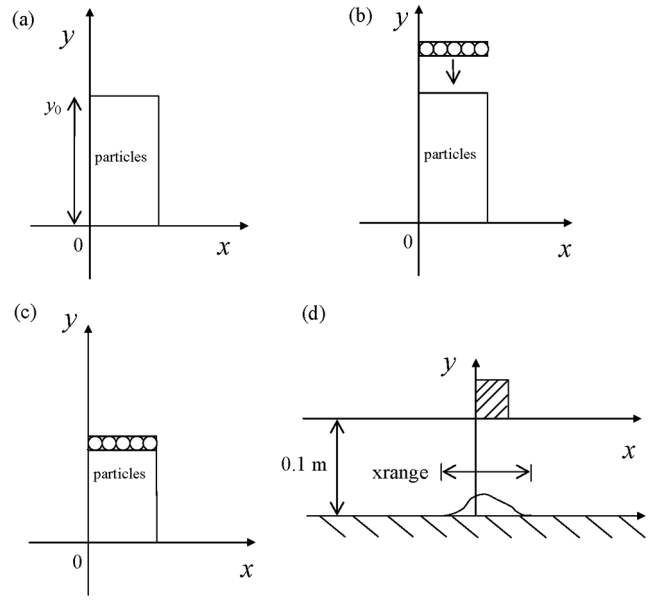


**Fig. 4.** Simulation procedure: (a) particles are added randomly into a rectangular container and allowed to settle, reaching a fill height $y_0$; (b) a rigid particle wall compresses the particles; (c) the particles are allowed to resettle. In (d), the "initialised" particles from (c) are released from rest 0.1 m above the bumpy base.

integrated successively to obtain new values for velocity and displacement. Performing this for all particles at that time-step results in an updated set of position and velocity information. This procedure is repeated for a series of small time-steps, allowing the simulation to progress forward in time.

## 3.2 Simulation description

Figure 1 shows the general steps in the numerical simulation. The process is meant to be similar to when sediment tailings leftover from nodule harvesting are released back into the sea. However we cannot simulate a continuously large flow of particles and hence have simplified the procedure: we release a lightly compacted collection of particles from a short distance above a horizontal surface.

First we "initialise" the system —*i.e.*, create the collection of particles pre-release. Particles (450 circles of 1 mm diameter, with density 2400 kg/m$^3$, Young's modulus 30 MPa, Poisson's ratio 0.3) are "poured" randomly into a rectangular container with width 0.01 m and height 0.1 m (fig. 4(a)) and allowed to settle in the container until the average kinetic energy is at a minimum, typically reaching a height of $y_0 = 0.045$ m. Next, a rigid wall made up of particles (5 circles with 2 mm diameter, with material density 2400 kg/m$^3$) is used to compress the particles (fig. 4(b)). The particles are then allowed to resettle for a given time (fig. 4(c)). We consider this compressed and resettled state as the initialised state of the particles. In this work, the main purpose is to set a reasonable model to simulate the motion of the sediments. The effects of the amount of compression and initial solid fraction are considered in a following work.

Next, the lightly compacted particles are allowed to fall from rest through a quiescent medium with the same properties as water (density = 1030 kg/m$^3$, viscosity = $1.08 \times 10^{-3}$ Pa s) from a distance of 0.1 m above the base (fig. 4(e)). It must be noted that although we have fixed the far-field fluid velocity to be zero, the fluid velocity in the vicinity of a particle can be non-zero if the Stokeslet disturbance is included in the force model, which we detail in sect. 3.3. Circles of 2 mm diameter, fixed rigidly in space, form the rough bottom boundary in the simulation. As with the experiments, we use "xrange" to denote the horizontal spreading of the particles throughout the simulation.

The time-step size for all the simulations is $5 \times 10^{-6}$ s, and we calculate the local solid fraction $\phi$ of a particle as follows:

$$\phi = \frac{A_P}{A_T} = \frac{n\pi d^2/4}{10d \times 10d}, \tag{3}$$

where $A_T$ is an area in space with dimensions $10d$ by $10d$ (equivalent to $0.01 \times 0.01$ m$^2$ for $d = 1$ mm), and $A_P$ is the area of the $n$ particles whose centres fall within the borders of the space.

## 3.3 Force models

The motion of each particle $i$ is governed by Newton's 2nd Law of Motion

$$m_i \frac{\mathrm{d}v_i}{\mathrm{d}t} = \sum_{j=1}^{N} \mathbf{F}_{ij}^c + \mathbf{F}_i^f + \mathbf{F}_i^g, \tag{4}$$

where $m_i$ and $v_i$ are the mass and velocity of the $i$-th particle, $\mathbf{F}_{ij}^c$ is the force exerted by the $j$-th particle on the $i$-th particle, and $\mathbf{F}_i^f$ and $\mathbf{F}_i^g$ are the fluid effects and gravitational force, respectively. Section 3 contains details on the particle-particle interaction force $\mathbf{F}_{ij}^c$, while the rest of this section will describe how the effects of the fluid will be modelled via the force term $\mathbf{F}_i^f$.

Table 2 summarises the force models used, and the main differences between them.

### 3.3.1 Concentration-dependent hydrodynamic drag

For this model the fluid effects have two components —the drag force $\mathbf{F}^d$ and buoyancy $\mathbf{F}^b$, which are expressed as follows:

$$\mathbf{F}_i^f = \mathbf{F}^d + \mathbf{F}^b = -C_d \frac{\rho_f |(\mathbf{v}_i - \mathbf{u}_i)|(\mathbf{v}_i - \mathbf{u}_i)}{2} A + m_f \mathbf{g}, \tag{5}$$

where $A$ is the projected "area" of the particle normal to the relative velocity, $m_f$ is the mass of fluid (with density $\rho_f$) taking up the same space as the particle, $d$ is the particle diameter, $\mathbf{v}_i$ is the velocity of the $i$-th particle, $\mathbf{u}_i$ is

**Table 2.** Comparison of fluid force models.

| Model | Drag force | Added mass | Stokeslet disturbance |
|---|---|---|---|
| 1 | Concentration-dependent hydrodynamic drag | no | no |
| 2 | Concentration-dependent hydrodynamic drag | $C_m = 0.5$ | no |
| 3 | Concentration-dependent hydrodynamic drag | $C_m = (1+2\phi)/(1-\phi)$ | no |
| 4 | Concentration-dependent hydrodynamic drag | $C_m = 0.5$ | yes |
| 5 | Stokes' drag | no | no |
| 6 | Stokes' drag | $C_m = 0.5$ | yes |

the fluid velocity at $\mathbf{x}_i$, $\mathbf{g}$ is the gravitational acceleration and $C_d$ is the drag coefficient defined as

$$C_d = \left(0.63 + \frac{4.8}{\sqrt{\mathrm{Re}}}\right), \tag{6}$$

where the particle Reynolds number is

$$\mathrm{Re} = \frac{\rho_f d|\mathbf{v}_i|}{\mu}, \tag{7}$$

and $\mu$ is the fluid viscosity. For a constant size $d$ and all the particles starting out in a similar state, the drag force experienced by each particle as they move through the fluid is the same. In other words, the influence of the other, neighbouring, particles on the drag force of an individual particle is not considered. Such a model would be trivial, and hence we consider instead a model where the drag coefficient varies with local solid fraction [14].

Here, the drag force $\mathbf{F}^d$ is modified by adding a voidage function $g(\varepsilon)$ to the original expression $\mathbf{F}_0^d$,

$$\mathbf{F}^d = \mathbf{F}_0^d\, g(\varepsilon) = -C_d \frac{\rho_f |(\mathbf{v}_i - \mathbf{u}_i)|(\mathbf{v}_i - \mathbf{u}_i)}{2} \frac{\pi d^2}{4} \varepsilon^{-\beta}, \tag{8}$$

where $\varepsilon$ is the local void fraction, and its exponent is defined as

$$\beta = 3.7 - 0.65 \exp\left[-\frac{(1.5 - \log(\mathrm{Re}))^2}{2}\right]. \tag{9}$$

For a single particle, the voidage fraction approaches one, reducing the drag force back to the usual hydrodynamic drag. Inversely, as the local solid fraction (the concentration) increases, the void fraction decreases (because the concentration and the void fraction sum to one), resulting in the function $g(\varepsilon)$ increasing exponentially.

### 3.3.2 Concentration-dependent drag with added mass

In this model a third component, known as the added mass, is introduced into the fluid effects term to model the resistance experienced by the particle when accelerating the fluid in its immediate surroundings

$$\mathbf{F}_i^f = \mathbf{F}^d + \mathbf{F}^b + \mathbf{F}^m. \tag{10}$$

The added mass component is usually incorporated into the governing equation on the left-hand side, written as

$$(m_i + C_m m_f)\frac{\mathrm{d}v_i}{\mathrm{d}t} = \sum_{j=1}^{N} \mathbf{F}_{ij}^c + \mathbf{F}^d + \mathbf{F}^b + \mathbf{F}_i^g. \tag{11}$$

This expands to:

$$(m_i + C_m m_f)\frac{\mathrm{d}v_i}{\mathrm{d}t} = \sum_{j=1}^{N} \mathbf{F}_{ij}^c - \frac{1}{2} C_d \rho_f \left|(\mathbf{v}_i - \mathbf{u}_i)\right| (\mathbf{v}_i - \mathbf{u}_i) \frac{\pi d^2}{4} \varepsilon^{-\beta} + (m_f - m_i)\mathbf{g}, \tag{12}$$

where $C_m$ is the added mass coefficient.

There is no standard value for the added mass coefficient. The particle mass was increased by 20% to account for the fluid mass in [26, 27], which resulted in $C_m = 0.5$ (assuming that the solid-fluid density ratio was 2.5). It is found experimentally that the added mass varied with local solid fraction, and $C_m = (1+2\phi)/(1-\phi)$ was proposed [13], where $\phi = 1 - \varepsilon$, is the particle fraction. We will consider both these models in this paper.

### 3.3.3 Uniform added mass, concentration-dependent drag, and Stokeslet disturbance superposition

This model is the most complicated of the models involving hydrodynamic drag so far, as it includes an attempt to account for the effect of moving neighbours on the fluid velocity in the immediate vicinity of a specific particle. Even in a quiescent flow, there are fluid particles moving as a result of the motion of a single particle falling under gravity. For a group of particles, the motion at any point in a fluid will, logically, be the collective result of all the surrounding solid particles influence.

We can think of a Stokeslet disturbance as the effect on the ambient fluid velocity of a single particle; the resultant effect due to a collection of particles is then the summation of the Stokeslet disturbances contributed by the neighbouring particles. The superposition is weighted by the proximity of the particles via the Stokeslet tensor $\mathbf{w}(\mathbf{x}_i; \mathbf{x}_j)$, such that the effect is diluted for particles further away from the point of consideration. At the centre

of mass of the $i$-th particle $\mathbf{x}_i$, the disturbed fluid velocity $\mathbf{u}_i^f$ is approximated as

$$\mathbf{u}_i^f = \sum_{j\neq i} \mathbf{w}(\mathbf{x}_i;\mathbf{x}_j) 3\pi\mu d \left(\mathbf{v}_j - \mathbf{u}_j^f\right), \tag{13}$$

where $\mathbf{v}_j$ is the velocity of the neighbouring $j$-th particle, $1 \leq j \leq N$ and $\mathbf{u}_j^f$ is the fluid velocity at $\mathbf{x}_j$ in the absence of the $j$-th particle, from the previous time-step. The Stokeslet tensor is given by

$$\mathbf{w}(\mathbf{x}_i;\mathbf{x}_j) = \frac{1}{8\pi\mu}\left(\frac{\mathbf{I}}{|\mathbf{x}_i - \mathbf{x}_j|} + \frac{(\mathbf{x}_i - \mathbf{x}_j)(\mathbf{x}_i - \mathbf{x}_j)}{|\mathbf{x}_i - \mathbf{x}_j|^3}\right), \tag{14}$$

where $\mathbf{x}_j$ is the centre of mass of the $j$-th particle and $\mathbf{I}$ is the identity tensor. The above expression for the fluid velocity $\mathbf{u}_i^f$ is then used in the concentration-dependent drag term, so that the full governing equation is as follows:

$$\begin{aligned}&(m_i + C_m m_f)\frac{\mathrm{d}v_i}{\mathrm{d}t} = \\ &\sum_{j=1}^{N} \mathbf{F}_{ij}^c - \frac{1}{2}C_d\rho_f \left|\left(\mathbf{v}_i - \mathbf{u}_i^f\right)\right| \left(\mathbf{v}_i - \mathbf{u}_i^f\right) \frac{\pi d^2}{4}\varepsilon^{-\beta} \\ &+\frac{\pi d^3}{6}(\rho_f - \rho)\mathbf{g},\end{aligned} \tag{15}$$

where a constant value for the added mass coefficient $C_m = 0.5$ is employed, and the drag varies with the local solid concentration.

For this model, a special treatment is required to model the Stokeslet disturbance contributed by the wall. This is done by introducing "mirror" particles, *i.e.*, when the particles are within a specified proximity to the wall, virtual particles are introduced which are reflections of the actual particles. The presence of the "mirror" particles results in the mutual Stokeslet disturbances cancelling out exactly along the wall. However when the particles are close enough to the wall, the Stokeslet disturbance from their reflected counterparts results in a very large repulsion force, which causes the particles to bounce. Hence, we only introduce the "mirror" particles when the falling particles are $10d$ (0.01 m) away from the wall. The Stokeslet disturbance resulting from the real particles is only considered when the particles are away from the wall with minimum distance $5d$ (0.005 m). We describe the implementation of the Stokeslet disturbance and "mirror" particles with greater detail in the appendix.

#### 3.3.4 Stokes' drag

Considering that the simulated system will be mostly laminar, then Stokes' drag may be more appropriate than the hydrodynamic drag

$$\mathbf{F}^d = -3\pi\mu d\left(\mathbf{v}_i - \mathbf{u}_i^f\right). \tag{16}$$

It should be noted that Stokes' drag is valid only for vanishing solid fraction. The governing equation for this model is

$$m_i\frac{\mathrm{d}\mathbf{v}_i}{\mathrm{d}t} = \sum_{j=1}^{N}\mathbf{F}_{ij}^c - 3\pi\mu d\left(\mathbf{v}_i - \mathbf{u}_i^f\right) + \frac{\pi d^3}{6}(\rho_f - \rho)\mathbf{g}. \tag{17}$$

#### 3.3.5 Uniform added mass, Stokes' drag, and Stokeslet disturbance superposition

This model is nearly identical to that in sect. 3.3.3, but with Stokes' drag instead of hydrodynamic drag. A constant added mass coefficient $C_m = 0.5$ is applied here again, but the drag force is independent of local solid concentration. The governing equation for this force model is then

$$\begin{aligned}&(m_i + C_m m_f)\frac{\mathrm{d}\mathbf{v}_i}{\mathrm{d}t} = \\ &\sum_{j=1}^{N}\mathbf{F}_{ij}^c - 3\pi\mu d\left(\mathbf{v}_i - \mathbf{u}_i^f\right) + \frac{\pi d^3}{6}(\rho_f - \rho)\mathbf{g}.\end{aligned} \tag{18}$$

Here, as with the model described in sect. 3.3.3, we introduce the "mirror" particles when the falling particles are $10d$ (0.01 m) away from the wall. The Stokeslet disturbance resulting from the real particles is only considered when the particles are away from the wall with minimum distance $5d$ (0.005 m). A more detailed description of the Stokeslet disturbance and "mirror" particles implementation is included in the appendix.

### 3.4 Numerical simulation results

Figure 5 plots the horizontal spread (top row), average vertical displacement (middle row) and average vertical velocity (bottom row) against time, for each of the six fluid force models. For the concentration-dependent hydrodynamic drag model (model 1), the particles settle down at $t \sim 1.5$ s, which is shown in both the average vertical displacement and average vertical velocity. The increase of the horizontal spread occurs in two main stages: the initial stage (0–0.1 s), and the settling stage (1.2–1.5 s). In the initial stage, the particles separate due to the initial compression and resultant repulsive forces between particles. The horizontal spreading reaches approximately 0.06 m after settling fully; the average vertical velocity remains approximately constant at $\sim -0.1$ m/s except for the initial acceleration and settling periods. This is due to the relatively large drag force applied in model 1, which increases with higher particle concentration, enabling the particles to reach the terminal velocity quickly.

In models 2 and 3, the added mass force is incorporated with the added mass coefficient $C_m = 0.5$ and $C_m = (1 + 2\phi)/(1-\phi)$, respectively. There is no significant qualitative difference among the results of models 1–3, except that the introduction of added mass causes the settling process to

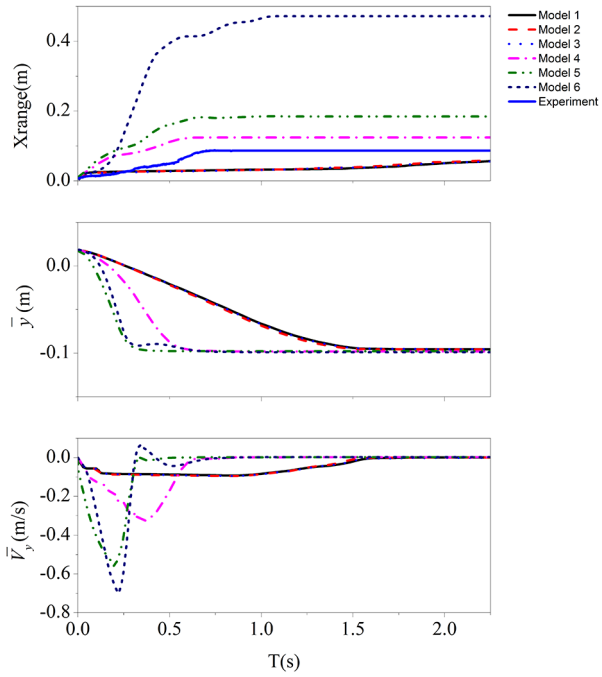


**Fig. 5.** Evolution of the horizontal spreading (top row), average vertical position (middle row) and vertical velocity (bottom row) with time for each model.

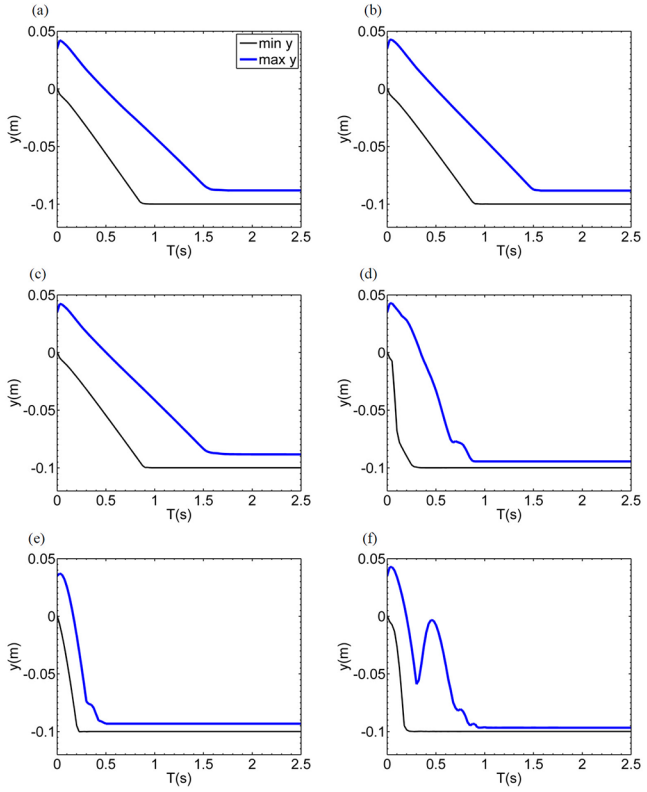


**Fig. 6.** Maximum (thick blue line) and minimum (thin black line) $y$-coordinates of the particles against time. Parts (a)–(f) correspond to models 1–6.

be slightly faster. At first, this seems counterintuitive — added mass should be akin to additional drag, causing the particles not to accelerate as much. This is certainly true, however the resistance presented by the added mass will be more evident later in fig. 6.

The behaviour of the system for the concentration-dependent hydrodynamic drag force model with Stokeslet disturbance (model 4) is qualitatively similar to the previous three models in terms of the horizontal spreading and average vertical position, except that the process takes place in approximately half the time ($\sim 0.8\,$s for the particles to settle down). However a closer look at the average vertical velocity shows a larger magnitude (the maximum value achieved is $\sim -0.4\,$m/s) and an absence of the velocity plateau, which implies that the resistance experienced by the particles was slower to build up —allowing greater velocities to be achieved— and the particles settled on the base before reaching the terminal velocity. Another reason for the greater velocity is the Stokeslet disturbance, whereby the motion of the particles affects the surrounding fluid, which in turn provides additional acceleration for the nearby particles.

The two models involving Stokes' drag (models 5 and 6) are qualitatively similar to model 4, but both systems settle faster ($\sim 0.3\,$s for model 5 and $\sim 0.4\,$s for model 6), spread more, and achieve greater vertical velocities. The Stokes' drag model (model 5) spreads to $\sim 0.2\,$m, which is a longer distance compared to the concentration-dependent hydrodynamic drag model (model 1), and the average vertical velocity reaches a maximum of $\sim -0.1\,$m/s before decelerating. When a constant added mass and Stokeslet disturbance is added into the fluid force model (model 6), the particles first reach the bottom at $\sim 0.4\,$s, with a maximum average vertical velocity of $-0.7\,$m/s, reaching a horizontal spread of $\sim 0.5\,$m. The greater velocities exhibited with these force models are as expected, since Stokes' drag generally has a smaller magnitude compared to concentration-dependent hydrodynamic drag.

The effect of the Stokeslet disturbance superposition is more obvious when comparing the models using hydrodynamic drag (model 3 and 4) —the average velocity increases faster and to a greater magnitude, such that the particles settle faster. The horizontal spread is also larger, which is another indication that the overall resistance experienced by the particles is smaller.

Comparing hydrodynamic drag to Stokes' drag (models 1 and 5), we observe that Stokes' drag appears to be of a smaller magnitude than the concentration-dependent hydrodynamic drag —the average velocity increases faster and to a greater magnitude, resulting in a smaller settling time. The horizontal spread is also larger. This is also seen in models 4 and 6, after including the added mass effect as well as Stokeslet disturbance superposition.

Figure 5(a) also includes the experimental data for the evolution of horizontal spreading. We observe that there is a monotonic increase, eventually reaching a plateau (when the particles have fully settled) at about 0.75 s. In terms of magnitude, models 1–3 underestimate this spreading, while the others overestimate it. Model 4 is the closest in magnitude, with a difference of $\sim 0.038\,$m.

**Table 3.** Particle settling times.

| | $T_1$ (s) | $T_2$ (s) | $T_2 - T_1$ (s) |
|---|---|---|---|
| Model 1 | 0.85 | 1.58 | 0.73 |
| Model 2 | 0.90 | 1.50 | 0.60 |
| Model 3 | 0.90 | 1.60 | 0.70 |
| Model 4 | 0.23 | 0.83 | 0.60 |
| Model 5 | 0.23 | 0.50 | 0.27 |
| Model 6 | 0.18 | 0.88 | 0.70 |
| Experiments | 0.47 | 0.95 | 0.47 |

Figure 6 gives an indication of the vertical size of the particle cloud by plotting the maximum (thick blue line) and minimum (thin black line) $y$-coordinates of the particles against time, for each model. By comparing the vertical distance between the two lines, we can observe how the collection of particles spreads vertically during its falling process. In general the two lines are qualitatively similar, which implies that the collection of particles mostly fall and settle as a cohesive whole.

Closer inspection, however, shows that for the hydrodynamic drag models (models 1–4, figs. 6(a)–(d)) the distance between the two lines increases, showing that the higher particles fall slower than those below them. This probably contributed to the smoother piling and settling process upon reaching the bottom. Figure 6(d) exhibits a small peak in the maximum $y$-coordinate towards the end of the settling (at $\sim 0.6$–$0.9$ s), which represents the bouncing of particles due to the treatment of the wall for the Stokeslet disturbance superposition as described in sect. 3.3.3.

On the other hand, it can be observed that for the Stokes' drag model (model 5, fig. 6(e)) the distance between the two lines decreases, which means that the higher particles fall faster than the earlier particles. There is a small hitch in the maximum $y$-coordinate line towards the end of the falling process (at $\sim 0.3$–$0.4$ s) indicating where the later particles reach the accumulating pile of particles, and slow down before they settle.

At first glance, the addition of the Stokeslet disturbance (model 6, fig. 6(f)) results in some very qualitatively different behaviour —instead of a mostly monotonic decrease in the maximum $y$-coordinate, there are a few local peaks indicating bouncing. This is because there is additional acceleration contributed by the Stokeslet disturbance, which the relatively small Stokes' drag cannot fully balance. As a result the particles have a high velocity when they impact the base, leading to the bouncing exhibited. This is non-representative of physical reality, as seen when compared to the physical experiment results, and hence we do not take measurements from this figure for comparison with the others.

We use $T_1$ to denote the time at which the particles first contact the bottom, and $T_2$ to denote the time at which all the particles have settled and are stationary. Table 3 lists the values of $T_1$ and $T_2$ for all six models. Due to the initial compression and the shape of the container, a portion of the sand sometimes becomes slightly jammed in the container in the experiments. Thus, the sand does not escape smoothly from the container as a single cluster when released underwater. As a result, it can take longer for all the sand to fully settle down in the experiment than in the numerical simulations. However, the time taken for the sand to first reach the bottom is unaffected, so we can compare $T_1$ when comparing the settling times of the experiment and the numerical results. The average $T_1$ for the experiments is 0.47 s.

Due to the relatively large concentration-dependent drag force, models 1–3 (figs. 6(a)–(c)) have a distinctly larger $T_1$ and $T_2$ as compared to the other models. The effect of the added mass is also exhibited here —comparing models 1 and 2, the increased resistance from the added mass causes $T_1$ for model 2 to be larger than that of model 1. This does not hold true for the whole collection of particles however, as the final settling time $T_2$ is greater for model 1 than for model 2. However, the form of the added mass coefficient affects the final settling time —$T_2 = 1.5$ s for $C_m = 0.5$ (model 2, fig. 6(b)) and 1.6 s for $C_m = (1 + 2\phi)/(1 - \phi)$ (model 3, fig. 6(c)).

Superposition of the Stokeslet disturbance also affects the settling time, but in a less significant manner. For the hydrodynamic drag models (models 3 and 4, figs. 6(c) and (d)), both $T_1$ and $T_2$ are smaller when the Stokeslet disturbance is considered; the overall time needed to settle is only slightly decreased, however. Comparing models 5 and 6 (figs. 6(e) and (f)) for Stokes' drag models, we see that with the Stokeslet disturbance the first particle reaches the bottom slightly faster than without. We cannot compare the final settling time, as the bouncing in model 6 (fig. 6(f)) results in an overestimate of $T_2$.

Figure 7 shows snapshots of the simulations in progress for the concentration-dependent hydrodynamic drag model (model 1), concentration-dependent drag with constant added mass and Stokeslet disturbance superposition (model 4), and both Stokes' drag models (models 5 and 6), while fig. 8 shows the corresponding vertical velocity and local solid fraction of all the particles in each system at the same times. These times of the snapshots were chosen to be representative of the simulations' progress: at the beginning, after release; in the middle of the falling/settling process; and lastly when the particles are mostly settling.

When the drag force is concentration-dependent (model 1, fig. 8(a)), the particles initially fall with a speed of $\sim -0.1$ m/s. At $T = 0.75$ s, the particles separate more compared to those at $T = 0.25$ s. Their velocities are approximately unchanged. This matches the appearance of the particles moving as a whole in fig. 7(a). At $T = 1.5$ s, most of the particles are settled, and no bouncing is observed. In all three snapshots, we observe that the qualitative profile of the vertical velocity and local solid fraction are similar —this implies that when the solid fraction is low, the vertical velocity is also low, and vice versa. This is not unexpected since the drag force is concentration-dependent. We note that both the vertical velocity and the local particle fraction are symmetric about $x = -0.005$ in-

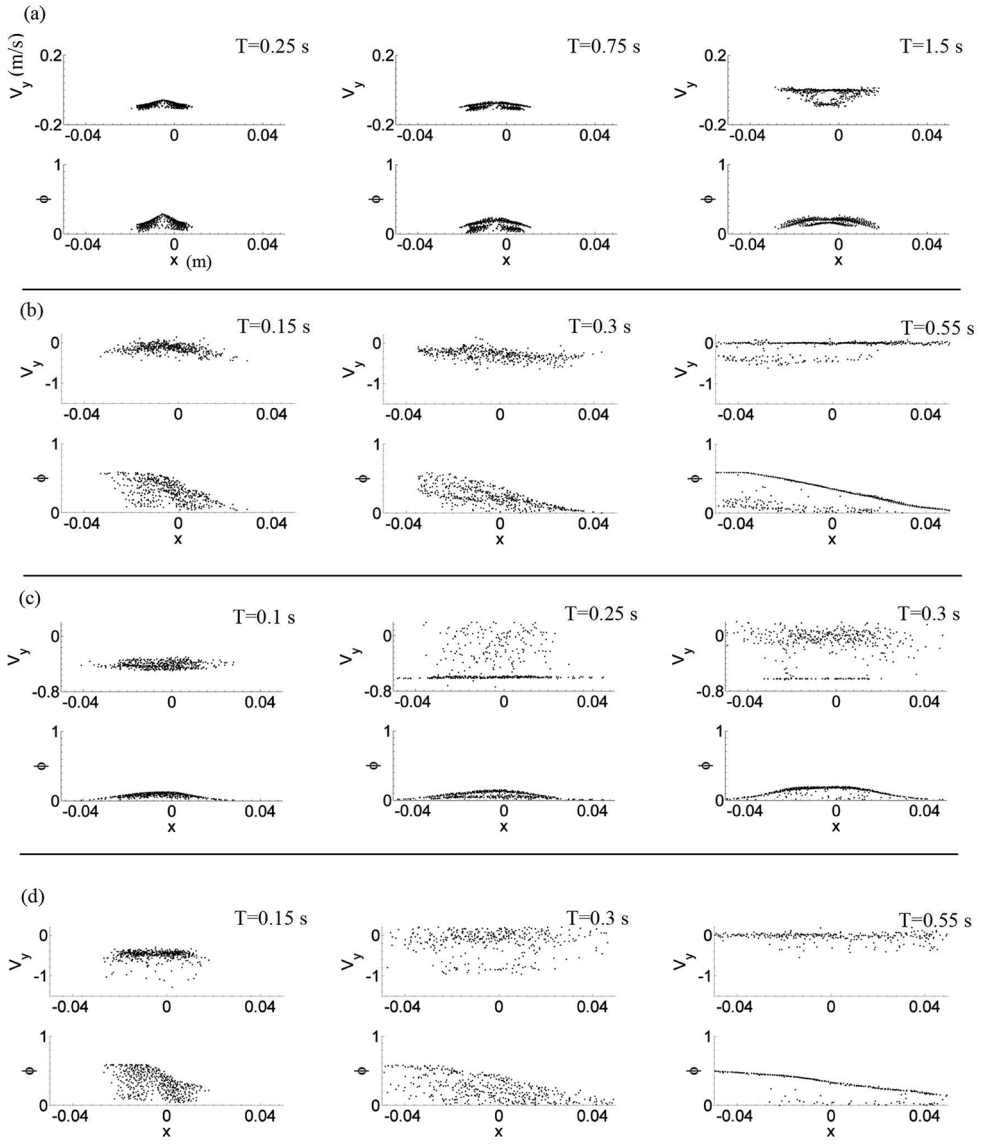


**Fig. 8.** Vertical velocity and local particle fraction of all particles for (a) model 1, (b) model 4, (c) model 5 and (d) model 6 at increasing time intervals.

stead of $x = 0$. This deviation is due to the non-symmetric separation of the particles after being released, rather than any external forces.

As for the Stokes' drag model results in figs. 7(c) and 8(c), we observe that the particle vertical velocities of the particles range from $-0.6$ to $-0.2\,\mathrm{m/s}$ for the Stokes' drag force model (model 5). The local particle concentration is relatively low when the particles are falling ($\phi < 0.2$). At $T = 0.25\,\mathrm{s}$, some particles reach the bottom and bounce, while other particles are still falling with high velocity. There are two distinct local solid fraction profiles shown —one bell-shaped curve corresponding to the already settled particles which are concentrating near $x = 0$, and the less concentrated particles which are still falling through the water, as can be seen in the snapshot. At $T = 0.3\,\mathrm{s}$, the vertical velocities of most particles are around 0, while a small proportion of the particles are still falling.

Comparing the two models involving Stokeslet disturbance (models 4 and 6, figs. 7(b) and (d), and 8(b) and (d)), it can be seen that at $T = 0.15\,\mathrm{s}$, the vertical velocity for model 6 is larger than that of model 4, which implies that the particles in model 6 reach the bottom faster than in model 4. At $T = 0.3\,\mathrm{s}$, the vertical velocities for model 4 are nearly unchanged meaning that the particles have already reached terminal velocity at $\sim 0.4\,\mathrm{m/s}$. However, the velocity distribution for model 6 is quite large, due to the inclusion of both Stokes' drag and Stokeslet disturbance. Finally, at $T = 0.55\,\mathrm{s}$, most particles have settled down. We observe that throughout the falling process, the local solid fraction does not have the same qualitative profile as the vertical velocity, implying that the influence of the solid fraction on the vertical velocity is not significant.

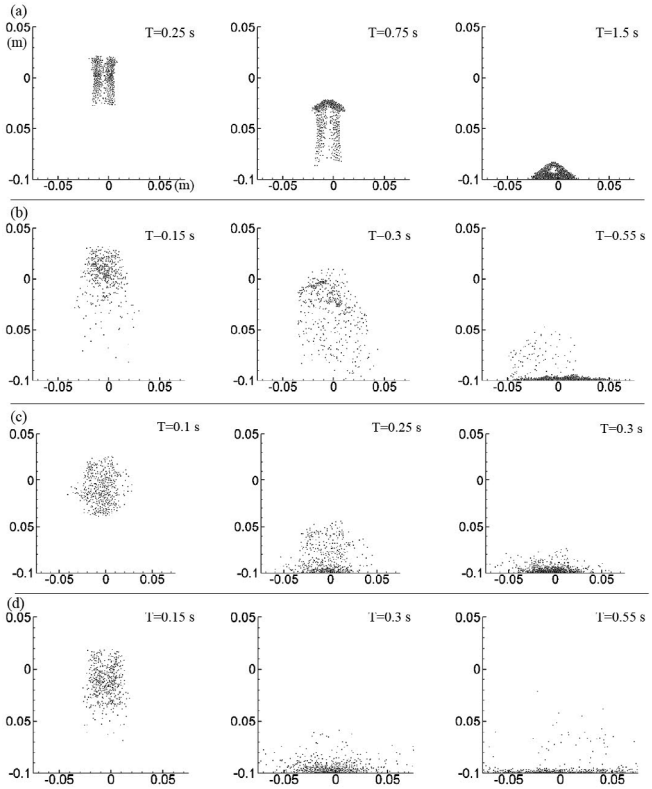


**Fig. 7.** Snapshots of the simulations for (a) model 1, (b) model 4, (c) model 5 and (d) model 6 at increasing time intervals.

**Table 4.** Features exhibited by numerical simulations.

| Model | Bouncing | Higher concentration moves faster | Wall effect |
|---|---|---|---|
| 1 | No | No | No |
| 2 | No | No | No |
| 3 | No | No | No |
| 4 | No | Yes | Yes |
| 5 | Yes | No | No |
| 6 | Yes | Yes | Yes |

## 4 Discussion

Basically, the outstanding features of the physical experiment are:

1) no obvious bouncing after the particles first make contact with the ground;
2) the particles in the center fall faster than those on the periphery of the cluster, resulting in a concentrated cluster surrounded by slower, less concentrated particles;
3) the proximity of the floor ("wall effect") causes the horizontal spreading (xrange) to increase.

The most realistic numerical simulation would exhibit all of the physical experiment's outstanding features for qualitative similarity; the settling time and horizontal spreading should also be of similar magnitude for quantitative similarity. We compare the features seen in the numerical simulations in table 4. Table 5 lists the radii of the circles formed by the settled particles in the numerical simulations.

**Table 5.** Radii of particle settling circles.

| | All particles (mm) | 90% particles included (mm) |
|---|---|---|
| Model 1 | 29 | 21 |
| Model 2 | 31 | 22 |
| Model 3 | 30 | 21 |
| Model 4 | 62 | 46 |
| Model 5 | 93 | 45 |
| Model 6 | 235 | 120 |
| Experiments | 38–42 | 32–36 |

We see that of all six models, model 4 (concentration-dependent hydrodynamic drag with constant added mass coefficient and Stokeslet disturbance superposition) captures all these characteristics and it is thus the most realistic model, qualitatively, for this particular system of non-cohesive spherical particles falling through a mostly quiescent fluid. However when comparing the data in table 5, model 4 spreads out into a much larger area (the radius is approximately 10 cm larger), while models 1–3 (concentration-dependent hydrodynamic drag with variations of added mass) are the closest to the physical experiment results quantitatively. Additionally, from table 3, model 4's particles first reached the base within half the time measured from the experiments, although the total time taken to settle was similar.

We believe that the reason for this difference in horizontal spreading between the "most realistic" force model 4 and the physical experiments is in the compaction of the granular material. As described in the simulation process, we apply a compaction to the particles so that the preparation process is similar to the physical process. However because the particles are spherical and cannot pack as well as the irregularly shaped real sand, this results in large interparticle repulsive forces (larger than in physical experiments). Thus the horizontal spreading in model 4 is significantly larger than in the physical experiments (see table 5 data) and therefore we cannot use xrange as a measure for the fluid force models' accuracy.

For our particular scenario, the force model 4 is the closest to physical reality; however it is reasonable to believe that the other models may be more appropriate in other situations. Models 2 and 3 (concentration-dependent hydrodynamic drag with added mass), for example, would be more realistic in systems where the solid-fluid interaction is significant. This includes fluid-sediment interaction in large seabed deformation, in which the added mass effect due to porous media (the seabed) is important [28]; and investigating sediment transport under oscillatory sheet flow, where added mass is an important

**Table 6.** Different settings for Zones I, II and III (vertical position $y$ given in mm.)

| Setting | Zone I | Zone II | Zone III |
|---|---|---|---|
| i | $y > 0$ | $0 \geq y > -5$ | $-5 \geq y > -10$ |
| ii | $y > 0$ | None | $0 \geq y > -10$ |
| iii | $y > 10$ | $10 \geq y > -5$ | $-5 \geq y > -10$ |
| iv | $y > -5$ | None | $-5 \geq y > -10$ |
| v | $y \geq -10$ | None | None |

component of the inter-particle force [29]. On the other hand, for fluid flows with very high Reynolds numbers and relatively large or rapid particle motions, the Stokeslet disturbance (included in models 4 and 6) should be considered as the solid particles may then affect local fluid characteristics greatly.

Another factor to consider is the local concentration of solid particles within the system. In our system, the local solid concentration varies in both time and space. Hence, force models 1–4 include concentration-dependent components. However there are cases in which it is possible that the local concentration could be assumed to have a relatively constant profile (depending on the time and length scales), for which such models would be more computationally expensive than needed. There exist empirical measurements which could be utilised —for example, the concentration profile of sand and bakelite grains were measured experimentally in sheet flow by Pugh and Wilson [30], the results of which have been used to study bedload sediment transport [31]; while Sumer *et al.* [32] investigated the concentration profile in sheet flow layer of movable beds. If it were reasonable to apply these measured profiles to the system of interest, then instead of a concentration-dependent force model a simpler version would be applicable.

## 5 Computational parameters

In this section, we investigate two of the computational parameters which may influence the simulation results —namely, the zone within which "mirror" particles are applied, as well as the relative significance of drag force in our "best" fluid force model (model 4, concentration-dependent hydrodynamic drag with constant added mass coefficient and Stokeslet disturbance superposition).

### 5.1 Mirror particles

We first briefly described our usage of "mirror" particles in sect. 3.3.3, and the appendix contains a more detailed explanation. There are three "zones" of importance here —Zone I is the area in which both real and "mirror" particles contribute Stokeslet disturbance to their neighbours; in Zone II only real particles have contributions; and lastly in Zone III Stokeslet disturbances are not considered at all.

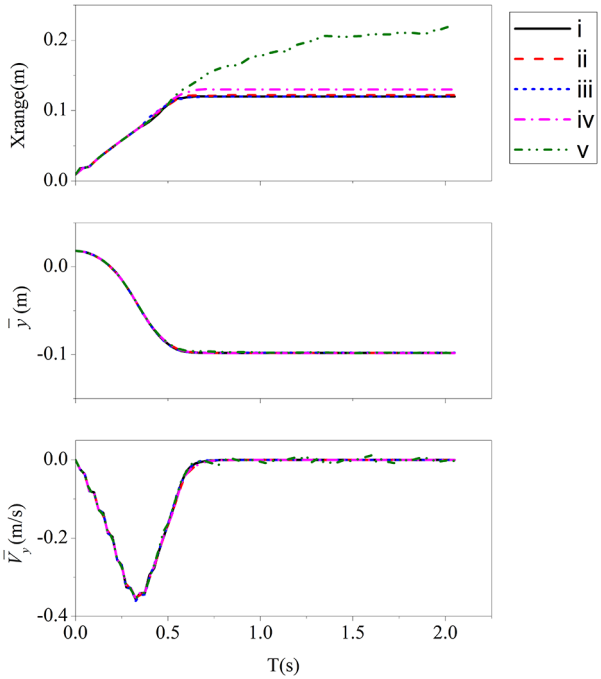


**Fig. 9.** Evolution of the horizontal spreading (top row), average vertical position (middle row) and vertical velocity (bottom row) in time for model 4 under different zone settings (see table 6).

Table 6 shows the different zone combinations we investigate here; our earlier presented results used combination i.

Figure 9 shows the horizontal spread (top row), average vertical position (middle row) and vertical velocity (bottom row) against time for model 4 under different zone settings. We see that:

1. The qualitative overall behaviour does not change significantly if the Stokeslet disturbance contribution from real particles is reduced slightly (comparing setting i to ii), or if the contribution from "mirror" particles is reduced slightly (comparing setting i to iii).
2. However, if the range of Zone I is increased, *i.e.* the contributions from a greater area containing "mirror" particles are considered (comparing setting i to iv), we observe that the horizontal spreading of the particles has increased slightly, while the average vertical position and average vertical velocity does not change much.
3. Finally, if the Stokeslet disturbance contributions from all existing real and "mirror" particles are considered (comparing setting i to v) then we observe a continuous increase in the horizontal spreading with time even after the particles have reached the base. This is due to the particles always being disturbed and never reaching a stationary state; something that is not observed empirically.

Given our observations, we believe that our choice of setting for Zones I, II and III (used for all the earlier presented results) does not have a significant effect on the simulation results. In fact, apart from v, all the tested settings i to iv give similar results.

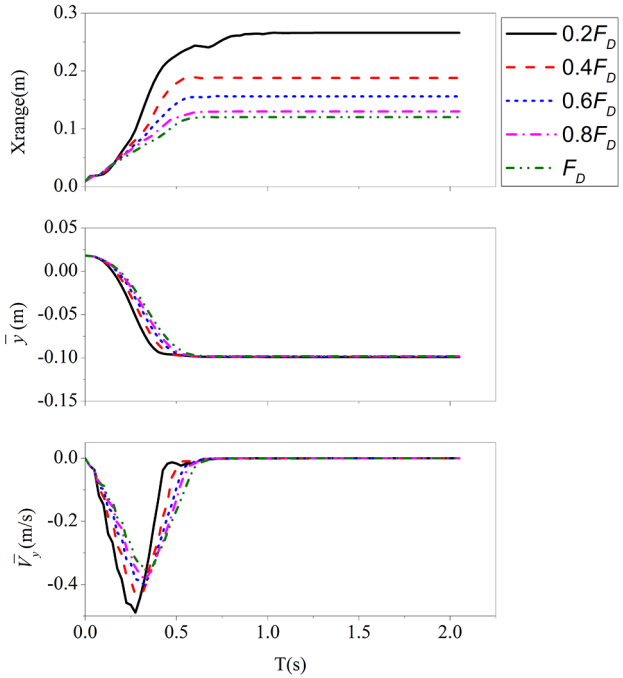


**Fig. 10.** Evolution of the horizontal spreading (top row), average vertical position (middle row) and vertical velocity (bottom row) against time for model 4, with the voidage function multiplied by a factor of 0.2, 0.4, 0.6, 0.8 and 1 (top to bottom).

### 5.2 Weighted drag force

The main features of the "best" fluid force model (model 4) are concentration-dependent hydrodynamic drag, constant added mass coefficient and Stokeslet disturbance superposition. In earlier comparisons we already observed the significance of introducing the added mass effect as well as the Stokeslet disturbance contributions. The only component that has thus not been investigated more closely is the drag force. It is undisputedly present, but given that the simulated particles are relatively small, then the significance of the drag force compared to the other two components in the fluid force model comes under question. Additionally, there are other factors which could affect the drag —particle shape or surface roughness, for instance— which have not been explicitly taken into account. Hence in this section, we apply an additional weighting factor to the drag force to artificially vary it, while keeping the other two components of the fluid force model unchanged. Figure 10 plots the horizontal spreading, average vertical position and vertical velocity against time for model 4, when the drag force is multiplied by a factor of 0.2, 0.4, 0.6, 0.8 and 1.0, respectively. We observe that as the drag force decreases (from v to i), the particles fall faster, reach the bottom earlier and generate a larger spreading area. This behaviour becomes more obvious when the drag force is very small. Of these observations, the first two are expected —reduced drag force naturally means that the particles can accelerate downwards faster. The increased spreading area follows directly as a consequence of the higher impact velocity. Overall, this shows that the simulation is very sensitive to the magnitude of the drag force.

From our earlier comparisons of the simulations to the experiments, we concluded that model 4 was the most realistic because it resulted in similar qualitative characteristics. However the overall dispersion process was faster (the particles reached the base faster) and the spreading distance was larger. Given the sensitivity to the magnitude of the drag force, this implies that model 4 can be made more realistic by increasing the drag force —thus reducing the particle velocity as well as the spreading distance. The need for an increased drag force can be explained by considering that real sand particles are not smooth or spherical, and thus would reasonably experience a larger drag force than the ideal circles of the simulations.

## 6 Conclusion

This paper modelled a collection of slightly compacted granular material, released at a short distance above a flat base in a quiescent fluid using the Discrete Element Method (DEM). Various fluid force models were used, with different drag force and added mass formulations as well as incorporation of Stokeslet disturbance. A simple physical experiment was carried out to validate the numerical simulations.

We observed that the outstanding features in the physical experiments were: no obvious bouncing, the particles in the centre fall faster than those on the periphery of the cluster, and the proximity of the floor causes the horizontal spreading to increase. This led us to conclude that for our current system of non-cohesive grains falling in a quiescent fluid, a sufficiently realistic simulation is achieved when the force model considers the local solid fraction in the drag force, and incorporates the hydrodynamic effect of neighbouring particles. This force model includes the added mass effect, but while it increases the accuracy of the outcome, it does not contribute significantly in a qualitative sense. For quantitative accuracy, the magnitude of the drag force should be increased, to account for the non-spherical shape of real sand particles as well as their rough surfaces.

Additionally, in the numerical simulations, the bouncing is greatly reduced by the large magnitude of the concentration-dependent hydrodynamic drag. The phenomenon whereby particles with higher local concentration move faster is effectively modelled by incorporating the hydrodynamic effect of neighbouring particles. Finally, we can simulate the non-penetration boundary condition of the wall, as well as the increased horizontal spreading in its proximity, by introducing "mirrored" particles.

The results we obtained in this work are very important in a few aspects: firstly, there is not a lot of literature comparing different DEM force models when applied to sediment in fluid; moreover, to the best of our knowledge, no force model incorporating concentration-dependent drag, Stokeslet disturbance and added mass has been used and compared with experimental data. A

force model which included Stokes' drag and Stokeslet disturbance was proposed in [22], however the drag force was independent of the local particle fraction and the added mass effect was ignored. Secondly, both the experiments and theoretical analysis improve our understanding of the underwater dispersion process, in particular the qualitative characteristics that are exhibited. By identifying the one force model which captures all the pertinent behaviour, we then learn which fluid forces are dominant in this process.

The authors would like to extend their gratitude to Prof. Phan-Thien Nhan and his research group for constructive feedback and discussion. This work was funded by the Singapore Ministry of Education (MOE) AcRF Grant, WBS no. R-265-000-508-133.

## Appendix A. Mirror particles & Stokeslet disturbance

Consider a pair of particles, of average diameter $d$. If the distance between them is very small, then each particle will induce a large Stokeslet disturbance at the other's position according to the following equations:

$$\mathbf{u}_i^f = \sum_{j \neq i} \mathbf{w}(\mathbf{x}_i; \mathbf{x}_j) 3\pi\mu d \left( \mathbf{v}_j - \mathbf{u}_j^f \right), \tag{A.1}$$

$$\mathbf{w}(\mathbf{x}_i; \mathbf{x}_j) = \frac{1}{8\pi\mu} \left( \frac{\mathbf{I}}{|\mathbf{x}_i - \mathbf{x}_j|} + \frac{(\mathbf{x}_i - \mathbf{x}_j)(\mathbf{x}_i - \mathbf{x}_j)}{|\mathbf{x}_i - \mathbf{x}_j|^3} \right). \tag{A.2}$$

Following this logic, falling particles should then induce large Stokeslet disturbances when they approach a solid wall (the floor, in fig. 11). However there should be no motion *along the plane of the wall*, so the Stokeslet disturbances are cancelled by introducing "mirror" particles which are reflections of the real particles about the wall. Since the mirror particles are only meant to model the non-penetration of the wall, then particles that are far away from the wall will not experience large repulsive forces even if they are in close proximity.

While the "mirror" particles can result in the solid wall being modelled perfectly, *i.e.* that particles exactly on the plane of the wall do not move or pass through it, this does not eliminate the fact that there are still very large Stokeslet disturbances experienced when the falling particles are close to, but not in contact with, the wall. This manifests as the particles bouncing on the wall, in numerical simulations. In order to reduce this unrealistic phenomena, we adopt the following measures:

1. The Stokeslet disturbance arising from the *real* particles are only considered when they are at a distance from the wall larger than $5d$ (0.005 m).
2. We only introduce the "mirror" particles when the falling particles are away from the wall at a distance larger than $10d$ (0.01 m).

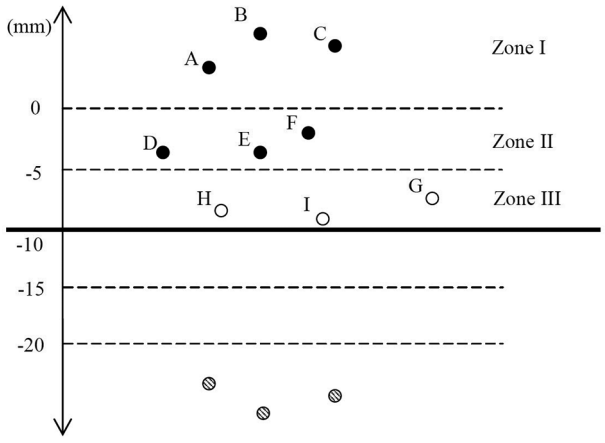


**Fig. 11.** Sketch showing the range of influence of "mirror" particles.

In other words, "mirror" particles contribute Stokeslet disturbances to any neighbouring particles only when their counterpart real particles are at a distance larger than $10d$ (0.01 m) away from the wall. When these real particles are within the range of $5d$–$10d$ away from the wall (*i.e.*, within 0.005–0.01 m) then they no longer have "mirror" particles, and thus only the real particles contribute Stokeslet disturbances. However when they are at less than $5d$ away, they no longer contribute Stokeslet disturbances.

Figure 11 illustrates this more clearly: particles A–F which are more than $5d$ away from the wall will contribute Stokeslet disturbances to their neighbours, while particles G–I do not. Particles A–C, being larger than $10d$ away from the wall, have "mirror" particles reflected about the wall ($x$-axis) and these "mirror" particles will contribute Stokeslet disturbances also.

## References

1. P. Hoogerbrugge, J. Koelman, Europhys. Lett. **19**, 155 (1992).
2. C. Marsh, *Theoretical Aspects of Dissipative Particle Dynamics* (University of Oxford, 1998).
3. E.G. Flekkøy, P.V. Coveney, G. De Fabritiis, Phys. Rev. E **62**, 2140 (2000).
4. P.A. Cundall, O.D. Strack, Geotechnique **29**, 47 (1979).
5. K. Hill, D.S. Tan, J. Fluid Mech. **756**, 54 (2014).
6. D. Salciarini, C. Tamagnini, P. Conversini, Phys. Chem. Earth, Parts A/B/C **35**, 172 (2010).
7. J. Calantoni, K.T. Holland, T.G. Drake, Philos. Trans. R. Soc. London Ser. A Math. Phys. Eng. Sci. **362**, 1987 (2004).
8. T.G. Drake, J. Calantoni, J. Geophys. Res.: Oceans (1978–2012) **106**, 19859 (2001).
9. Y. Tan, D. Yang, Y. Sheng, J. Eur. Ceram. Soc. **29**, 1029 (2009).
10. H. Kim, M.P. Wagoner, W.G. Buttlar, J. Mater. Civ. Eng. **20**, 552 (2008).
11. A. Damsgaard, D.L. Egholm, J.A. Piotrowski, S. Tulaczyk, N.K. Larsen, K. Tylmann, J. Geophys. Res.: Earth Surf. **118**, 2230 (2013).

12. J. Marshall, J. Comput. Phys. **228**, 1541 (2009).
13. N. Zuber, Chem. Eng. Sci. **19**, 897 (1964).
14. R. Di Felice, Int. J. Multiph. Flow **20**, 153 (1994).
15. C.Y. Wen, Y.H. Yu, Chem. Eng. Prog. Symp. Ser. **62**, 100 (1966).
16. S. Ergun, Chem. Eng. Process. **48**, 89 (1952).
17. H.G. Choi, D.D. Joseph, J. Fluid Mech. **438**, 101 (2001).
18. J. Zhang, L.-S. Fan, C. Zhu, R. Pfeffer, D. Qi, Powder Technol. **106**, 98 (1999).
19. B. Potic, S. Kersten, M. Ye, M. Van der Hoef, J. Kuipers, W. Van Swaaij, Chem. Eng. Sci. **60**, 5982 (2005).
20. L.v. Wijngaarden, D. Jeffrey, J. Fluid Mech. **77**, 27 (1976).
21. J.B.W. Kok, Doctoral Thesis, Twente University, The Netherlands.
22. J. Nitsche, G. Batchelor, J. Fluid Mech. **340**, 161 (1997).
23. J. Zhao, T. Shan, Powder Technol. **239**, 248 (2013).
24. M. van Sint Annaland, N. Deen, J. Kuipers, Chem. Eng. Sci. **60**, 6188 (2005).
25. S. Plimpton, J. Comput. Phys. **117**, 1 (1995).
26. T. Auton, J. Hunt, M. Prud'Homme, J. Fluid Mech. **197**, 241 (1988).
27. Z. Jiang, P. Haff, Water Resour. Res. **29**, 399 (1993).
28. T. Nakamura, S.C. Yim, J. Offshore Mech. Arct. Eng. **133**, 031103 (2011).
29. M. Li, S. Pan, B.A. O'Connor, Coast. Eng. **55**, 1159 (2008).
30. F.J. Pugh, K.C. Wilson, J. Hydraul. Eng. **125**, 117 (1999).
31. R.L. Soulsby, J.S. Damgaard, Coast. Eng. **52**, 673 (2005).
32. B.M. Sumer, A. Kozakiewicz, J. Fredsøe, R. Deigaard, J. Hydraul. Eng. **122**, 549 (1996).